Ultrasonics 94 (2019) 391–400

Contents lists available at ScienceDirect

Ultrasonics

journal homepage: www.elsevier.com/locate/ultras

Portable ultrasound imaging system with super-resolution capabilities

Swetha S. George, Michael C. Huang, Zeljko Ignjatovic*

University of Rochester, Rochester, NY, USA

ARTICLE INFO

Keywords:
Ultrasound
Portability
Compression
Super-resolution
Regularized deconvolution
Elastic nets

ABSTRACT

This paper discusses an ultrasound technique where the echo signals from the array of transducer elements are compressed to as few as two RF channels while still in analog domain, with a much simplified front-end electronics. The method can achieve resolutions well beyond the diffraction limit, which is set by the excitation signal wavelength and numerical aperture of the imaging system. The fundamental principle that underlies this model based imaging technique is the preservation of the spatial frequency information content of the recorded echo signals with the help of pseudo-random apodization function followed by summation. A Verasonics V1 ultrasonic scanner is used to conduct experiments using an anechoic cyst made from gel phantom, immersed in degassed water. The estimated images were compared to those obtained using traditional B-mode delay-and-sum imaging available with the Verasonics V1 ultrasound machine. The estimated images using the proposed imaging technique showed a contrast ratio of 0.96 and Full-Width-Half-Maximum (FWHM) of about half the wavelength at a depth of 9.1 cm and at 1.875 MHz center frequency while the traditional delay and sum images had a contrast ratio of 0.62 and FWHM of about 5.5 wavelengths.

1. Introduction

Super-resolution or subwavelength imaging has become a popular domain of research particularly in medical imaging. Over the past couple of decades, the world of imaging has seen drastic improvement in the resolution as well as image quality with the help of improved hardware and efficient image processing algorithms. Ultrasound is the preferred medical imaging modality in many clinical applications due to its non-ionizing, non-invasive and inexpensive nature. The need for achieving high resolution and contrast in ultrasound imaging comparable to MRIs or CT scans has fueled the extensive research aimed at improving the resolution and reducing artifacts present in ultrasound images. Today, a few companies have moved towards the handheld ultrasound market which will greatly benefit telemedicine and global healthcare.

The research presented in this paper is geared towards providing a design methodology that will enhance the resolution of ultrasound images *and* reducing the hardware requirements at the same time. This has been made possible with the help of compression methods and existing estimation techniques. Presently, there are many high resolution techniques but in the proposed ultrasound imaging technique, an effort has been made to integrate super-resolution along with compression. This integration allows for fewer number of channels and reduces the analog hardware footprint without compromising the resolution of the reconstructed images.

Therefore, the primary motivation for the work presented in this paper is to develop a technique for super-resolution and portable ultrasound imaging that involves simplified front-end electronics, reduced memory usage and lower computational cost in post-processing ends of the system. We refer to this novel technique as Ultrasound Coherent Imaging (UCI). In this work, we estimate ultrasound images based on a priori knowledge of a measurement matrix (or sensing matrix) as described in linear programming literature [1]. Echo signals received by the transducer elements are compressed to a fewer number of RF channels while still in analog domain greatly simplifying signal acquisition chain, as illustrated in our previous publications [2–4]. Thereafter, images are formed directly from the compressed RF data after only single plane wave excitation of the medium by assuming the imaging model to be a regularized inverse problem which can be solved using the elastic net regularization technique [5]. In addition, no beamforming is applied on receive in UCI. This is one of UCIs distinguishing features when compared to other super-resolution methods such as minimum-variance beamforming and deconvolution methods.

Section 2 briefly describes some literature related methods that achieve super-resolution and better contrast images. In Section 3, a brief overview of the concepts that underlie the UCI method is provided. This is followed by the simulation setup and results using Field II in Section 4. Section 5 describes the results from the experiment using a

---

* Corresponding author at: 419 Computer Studies Building, University of Rochester, Rochester, NY 14627, USA.
E-mail address: zeljko.ignjatovic@rochester.edu (Z. Ignjatovic).

https://doi.org/10.1016/j.ultras.2018.06.017
Received 25 January 2018; Received in revised form 31 May 2018; Accepted 26 June 2018

setup comprising of the Verasonics ultrasonic scanner, an ultrasound phantom in a water tank, and an ATL P4-1 transducer probe. And finally, a discussion of results in Section 6 and conclusion is presented in Section 7.

2. Related work

Over the past few years, techniques such as deconvolution [6,7] and adaptive/minimum-variance beamforming [8–12] have been extensively researched and applied to the field of medical imaging. Adaptive beamforming techniques have demonstrated improvement in image resolution with the help of reduced main lobe width and low sidelobe levels. Adaptive beamformers calculate the weights for receive apodization based on the recorded data rather than using pre-calculated values. The authors in [8,9] claim to achieve a better resolution compared to traditional delay-and-sum (DAS) beamformers while using a smaller aperture and parallel receive beamforming with their minimum variance method. All of these techniques described above aim to achieve ultrasound images that have better contrast or marginally better resolution by reducing the side lobes or by applying inverse filtering techniques.

Super-resolution (SR) or subwavelength imaging, on the other hand, aims at reducing the dependence of resolution on pulse shape and width as well as the presence of speckles in order to achieve higher resolution. There are numerous super-resolution techniques that obtain images by combining many low resolution images and applying post image processing techniques. Super-resolution through time reversal acoustics can also be achieved due to the random nature of inhomogeneous media [13,14]. The phase-coherent multiple signal classification (MUSIC) method described in [15] was able to improve the ultrasound resolution to 1/4th of a wavelength at frequencies in the 4–11 MHz range at a depth of a couple centimeters when the field of view is less than the transducer width. Another research group [16] concentrated on improving the temporal resolution and acquisition times seen in ultrasound localized microscopy by applying the super-resolution optical fluctuation imaging method. Research presented in [17] discusses a blind 2-D deconvolution technique based on an improved phase-unwrapping technique applied to the pulse estimation. Their images showed sharper tissue boundaries when compared to the images before deconvolution. Another group of authors [18] describe a methodology that consists of performing parametric modeling on the Fourier transform of the Hilbert transform of the RF data and achieving subwavelength resolution at higher frequencies (20 MHz in their results).

Component modeling of the ultrasound signals/medium has become a popular approach to achieve super-resolution. In [19], the raw RF signals are considered to be the sum of two components (strong reflectors and the speckle). This method reduces the side lobes while achieving compressibility by statistically modeling the components with a few parameters [20,21]. Another interesting modeling and characterization method of ultrasound signals is presented in [22], where the authors propose to use a dynamic beamforming to address multipath propagation and side lobe artifacts and improve contrast ratio. One of the key features of this method is their linearized scattering model that treats multipath propagation as waveforms originating from outside of the region of interest. The image reconstruction problem is convex in nature and is solved by applying elastic net regularization. The work presented in [23,24] is also another model based ultrasound image reconstruction algorithm which is based on assuming the region of interest to be divided into diffuse targets [25] and then solved for using a maximum a posteriori estimator. Another interesting work that poses beamforming as an inverse problem is described in [26]. The beamforming is done laterally at each range (or depth) rather than axially as is the case for conventional sector scanning. The beamformed data is related to the signal with the help of a direct model which is then solved using elastic net regularization. As a result, the authors were able to achieve 8–12 dB improvement in the contrast ratio compared to DAS systems. The advantages to using elastic net regularization over basis pursuit (L1-norm constrained) or least squares (L2-norm constrained) is given in the Section 3. The authors in [27] describe another subwavelength technique to image objects within the ultrasound focus over a field of view equal to the focal area. Their technique was able to estimate the size and location of the object at a few tens of millimeters depth with the help of Fourier spatial frequency spectrum analysis of the signals that is backprojected in the wavevector domain to the focal plane.

3. Theory

Finer details of an object are often recovered from the higher spatial frequencies [28]. In a way, the imaging system acts as a spatial filter where the resulting signal is a convolution between the tissue reflectivity function (TRF), $g(x)$, and the point spread function (PSF) of the acoustic imaging system, say $h(x)$. A mathematical model describing the imaging process is shown in (1), where $n(x)$ is imaging noise and $*$ is the convolution operator.

$$y(x) = h(x)*g(x) + n(x) \tag{1}$$

In the frequency domain, this equation becomes,

$$Y(\widetilde{f}\,) = H(\widetilde{f}\,)\,G(\widetilde{f}\,) + N(\widetilde{f}\,) \tag{2}$$

where H is called the modulation transfer function (MTF). $Y(\widetilde{f}\,)$, $G(\widetilde{f}\,)$, and $N(\widetilde{f}\,)$ are the Fourier transforms in the spatial frequency domain $(\widetilde{f}\,)$ of $y(x)$, $g(x)$, and $n(x)$, respectively. Due to the finite aperture size of the transducer, there is a low-pass cutoff frequency above which information is typically lost. Typically, the MTF has spectral notches (or zeros) rendering the convolution operation in (1) non-invertible. Consequently, only the spectral components of the TRF below the first spectral notch (i.e., spatial frequency components below the diffraction limit) can be uniquely recovered. During the measurement process in most imaging systems, only coarse features of the TRF are obtained, thus not being able to resolve the finer details. According to the results presented in [29], when a wave is reflected by a scatterer, it introduces high frequency spatial content which affects the spatial frequencies below the cutoff spatial frequency. As such, the problem of super-resolution is one that involves recovering the fine details of a TRF being imaged with the coarse measurements from the spectrum below the cutoff spatial frequency.

Work in [29,30] demonstrates that super-resolution can be achieved if certain conditions like positivity, compactness or sparsity are assumed for the support of a TRF during the process of image reconstruction. Often, this has been achieved with the help of a priori information as demonstrated in previous literature [31,27,30,23,19]. This a priori information in the form of a known imaging model also lays the foundation for the UCI method described in this paper.

In conventional DAS, only the magnitude of the received signal is used during image reconstruction to form each A-line in the image. But in UCI, both the phase and amplitude are used for the image reconstruction process. In the proposed technique, a plane wave is sent out from a transducer array and the received echoes are compressed and stored without applying beamforming and envelope detection, thus being able to preserve the phase information.

3.1. Model characterization of the imaging system

We now describe the receive operation in UCI. The schematic in Fig. 1 shows the flow of RF signals that are received at each active element of the transducer. For each of the N_c transducer elements, N_s time samples are received forming an RF data matrix $\mathbf{B}$ of size $N_s \times N_c$. These time samples are denoted as b_{ij} where i stands for the time sample and j indicates the transducer element number. In addition, a pseudorandom matrix Φ of 1's and 0's of the same size as $\mathbf{B}$ is generated and

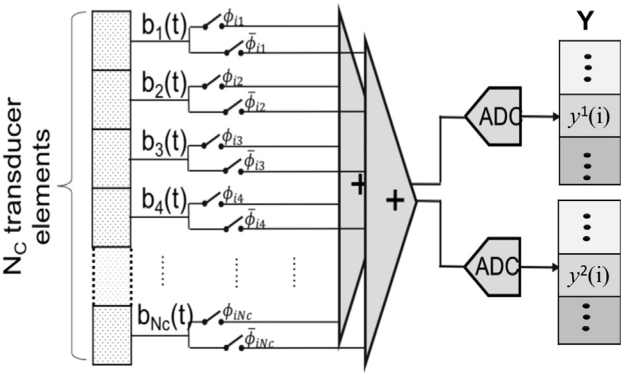

Fig. 1. Illustration of data acquisition in UCI.

stored in the memory.

At each time instant iT_s during the receive operation, where T_s is the sampling period, the transducer array generates an N_c-elements long row-vector $[b_1(iT_s)\ b_2(iT_s)...b_{Nc}(iT_s)]$. Furthermore, this row-vector represents an ith row of the matrix $\mathbf{B}$. Inner products between the row-vectors $\boldsymbol{b_i}$ and $\boldsymbol{\phi_i}$ as well as $\boldsymbol{b_i}$ and $\overline{\boldsymbol{\phi_i}}$ are then calculated, where $\boldsymbol{\phi_i}$ is the ith row of the matrix Φ and $\overline{\boldsymbol{\phi_i}}$ is the complementary vector of $\boldsymbol{\phi_i}$. The results are then stored as ith samples of the new compressed RF data vectors $\boldsymbol{y}^1$ and $\boldsymbol{y}^2$. In a way, the receive operation in the UCI can be described as a form of time-varying compressive beamforming. Even though there might be many ways to compress RF signals, our choice of this particular compression function provides several benefits. Firstly, the echo signal samples b_{ij} are combined by means of a simple pseudo-random modulation and summation operation. The use of pseudo-random modulation sequence helps to spread the information uniformly over the received frequency spectrum. Since the modulation compression sequence varies over different time and spatial samples, all point scatterers in the imaged medium are treated equally as opposed to traditional methods that focus at one scatterer at a time. This reduces front-end electronics to a simple switch matrix and two charge summation amplifiers, as shown in Fig. 1. And secondly, unlike other model based imaging algorithms such as qTONE [24], Aperture Domain Model Image REconstruction (ADMIRE) [22,32], the echo signal samples b_{ij} are compressed while still in analog domain, and only the results after compression are converted to digital signals and stored in memory. Therefore, the UCI significantly reduces the number of amplifiers and A/D converters from N_c to exactly two. In addition, it cuts down on the memory usage and lowers overall system complexity. Alternatively, the echo signal samples b_{ij} could be compressed by modulating rows of matrix $\mathbf{B}$ with pseudo-random vectors of 1's and -1's prior to the summation to a single channel, which is more commonly used in compression methods such as [2]. However, due to the fact that the echo signal samples are slow-varying across the array elements (i.e., in the lateral direction) for smaller numerical apertures, most of the signal power and SNR would be irreversibly lost. Therefore, the use of pseudo-random vectors of 1's and 0's and subsequent summation to two channels proves to be more appropriate for this particular application. The RF data compression in the UCI can be succinctly expressed as:

$$\begin{aligned}\boldsymbol{y}^1 &= (\mathbf{B}\circ\Phi)*\mathbf{1}\\ \boldsymbol{y}^2 &= (\mathbf{B}\circ\overline{\Phi})*\mathbf{1}\end{aligned} \tag{3}$$

where $\circ$ is a simple Hadamard product operation and $\mathbf{1}$ is a column vector of ones of size $N_c \times 1$. The vectors $\boldsymbol{y}^1$ and $\boldsymbol{y}^2$ are then concatenated to form the final vector of the target image, $\mathbf{Y}$ as shown in (4). The vector $\mathbf{Y}$ has dimensions that correspond to the number of compressed channels (see Fig. 1) times the number of samples, N_s, generated by each of the active array elements.

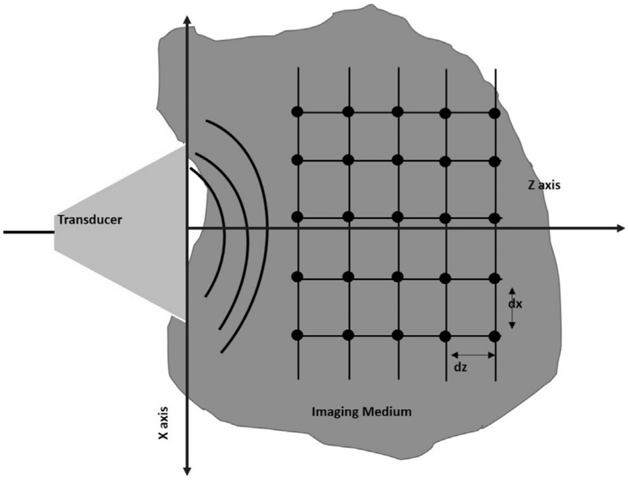

Fig. 2. Depiction of the grid overlaying the imaging medium.

$$\mathbf{Y}_{2N_s\times 1} = \begin{bmatrix}\boldsymbol{y}^1_{Ns\times 1}\\ \boldsymbol{y}^2_{Ns\times 1}\end{bmatrix} \tag{4}$$

It should be noted that this compression technique, described by (3) and (4), can be thought of as a linear time-variant spatial filter whose impulse response does not exhibit spectral notches allowing unique recovery of the phase and high-spatial-frequency components of the echo signals (i.e., the convolution operation in (1) becomes invertible).

We now describe the imaging model and image formation in the UCI. Consider the case of two dimensional imaging in the x-z plane where the axis of propagation is in the z direction (refer to Fig. 2). Given the transducer's field of view (FOV), a two dimensional grid is formulated to overlay the FOV with N_x and N_z as the dimensions in the x and z directions, respectively. The spacing between grid points in Fig. 2 along the x and z directions are denoted by dx and dz, respectively. The transducer is placed parallel to the x axis. As described in the introduction section, the image reconstruction method described in this paper is based on model characterization of the medium which we will refer to as the imaging matrix, $\mathbf{A}$. The matrix $\mathbf{A}$ can be described as a set of column vectors $\boldsymbol{a}_{2N_s\times 1}$ that correspond to the compressed RF signal received by the transducer array when only one point scatterer with maximum reflectivity is present in the FOV as shown in (5).

$$\boldsymbol{a}^{i+(j-1)N_x} = \begin{bmatrix}(\mathbf{B}^{\mathbf{ij}}\circ\Phi)*\mathbf{1}\\ (\mathbf{B}^{\mathbf{ij}}\circ\overline{\Phi})*\mathbf{1}\end{bmatrix},\ 1\leqslant i\leqslant N_x,\ \ 1\leqslant j\leqslant N_z \tag{5}$$

where $\mathbf{B}^{\mathbf{ij}}$ is the matrix of echo signals received by the transducer elements from a point scatterer located at (i, j) on the grid of size (N_x, N_z). Finally, the imaging matrix $\mathbf{A}$ is formed as shown in (6) and it is of size $2N_s$ by N_xN_z.

$$\mathbf{A} = [\boldsymbol{a}^1\boldsymbol{a}^2\cdots\boldsymbol{a}^{N_xN_z}]_{2N_s\times N_xN_z} \tag{6}$$

The imaging matrix, $\mathbf{A}$, is calculated prior to the process of imaging objects, and therefore it can be considered as a priori information about the imaging system.

3.2. Image estimation

The received and compressed RF signals from grid points of any TRF within the FOV will be a linear combination of the vectors in the imaging matrix $\mathbf{A}$. From here the image estimation problem can be formulated as a linear regression model as shown below.

$$\boldsymbol{y}_{2N_s\times 1} = \boldsymbol{A}_{2N_s\times N_xN_z}\boldsymbol{\beta}_{N_xN_z\times 1} + \boldsymbol{e}_{2N_s\times 1} \tag{7}$$

where $\boldsymbol{e}$ is white Gaussian noise, $\boldsymbol{y}$ is the received and compressed RF data from insonifying the target and $\boldsymbol{\beta}$ is the column vector of

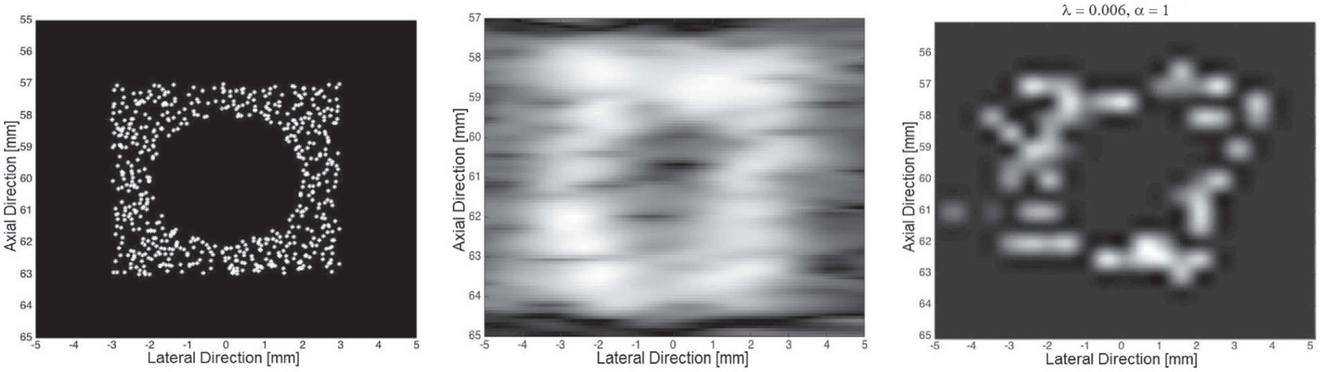

(a) Target Image (b) DAS Image. CR = 0.123, ER = -1.66 dB (c) α = 1, Lasso. CR=0.848, ER = -18.31 dB

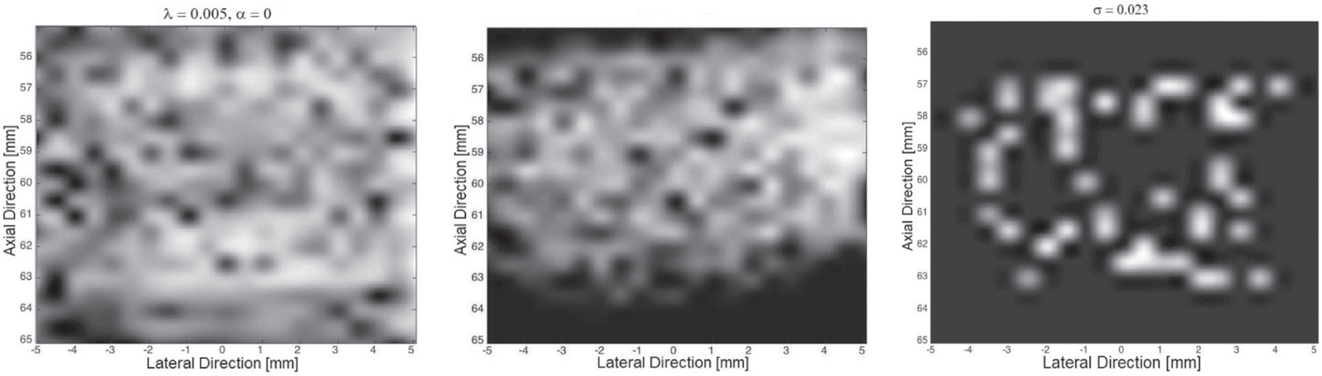

(d) $\alpha \approx 0$, Ridge Regression. CR=0.18, ER = -2.4 dB (e) Ordinary Least Squares. CR=0.082 (f) Iterative Reweighted Least Squares, CR=0.908, ER=-21.79 dB

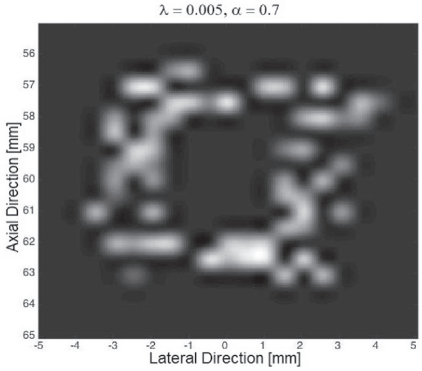

(g) Elastic nets. CR=0.929, ER=-35.5 dB

Fig. 3. A comparison of regularized estimation methods. The figure in (a) shows the target anechoic cyst phantom, (b) shows the conventional US image (c) shows the result when using lasso (d) shows ridge regression (e) OLS (f) IRLS. (g) Shows the image using elastic nets for a set of (α, λ).

reflectance coefficients to be estimated. Elements of the column vector $\boldsymbol{\beta}$ are arranged similar to the columns in the imaging matrix $\boldsymbol{A}$ where $(i + (j-1)N_x)$th element of $\boldsymbol{\beta}$ represents the reflectance coefficient for the grid point at (i, j).

As mentioned above, the estimation problem shown in (7) is the common linear regression model. A model-fitting procedure generates the coefficient matrix $\boldsymbol{A}$ of size $2N_s$ by N_xN_z. In other words, there are $p = N_xN_z$ predictors or variables to be estimated. One way to solve this problem is by finding the ordinary least squares (OLS) estimate by minimizing the residual sum of squares. But often, the matrix $\boldsymbol{A}$ is ill-conditioned when the number of predictors or variables is large compared to the number of observations. In such cases, the OLS estimation algorithm gives a small bias but large variance. This problem is especially pronounced when actual scatterers of the TRF are not aligned with any of the grid points, which would be expected in imaging real tissues. The resulting image exhibits large residual that is spread over a large area reducing resolution and contrast, as shown in Fig. 3(e). One possible solution to this ill-posed problem in the form of regularized least-squares was proposed by Hoerl and Kennnard [33]. The authors proposed the ridge regression technique which minimizes the residual sum of squares subject to a bound on the L2 norm of the coefficients, as shown in (8).

$$\hat{\boldsymbol{\beta}} = \underset{\beta}{argmin}(\|\mathbf{y}-\boldsymbol{A\beta}\|^2)\ s.\ t.\ \ \|\boldsymbol{\beta}\|^2 < \delta \tag{8}$$

Even though ridge regression provided better prediction models, it did not produce satisfactory contrast ratio in ultrasound images [34]. The main reason for the unsatisfactory performance of the ridge regression is that it tends to keep all the predictors in the model. What this means for ultrasound images is that when an anechoic structure such as a bladder is imaged, the model prediction will produce non-zero reflectance values within the structure. A subset selection method may be able to solve this problem since a sparser model is produced by keeping the predictors that exhibit stronger effects. Tibshirani [35] proposed the favorable lasso or least absolute shrinkage and selection operator in 1996. As explained in [35], it promotes sparsity, and thus is able to preserve the good features of both automatic variable selection and ridge regression. One drawback of lasso is that the method seems to perform poorly in case of high correlations between the variables. Another possible method of finding solution to the image reconstruction problem in (7) is based on iterative re-weighted least squares (IRLS) [36], as shown in (9), where λ is the regularization parameter and $\boldsymbol{D}$ is the weighting matrix [37].

$$\hat{\boldsymbol{\beta}} = \underset{\boldsymbol{\beta}}{argmin}(\|\mathbf{y}-\boldsymbol{A\beta}\|^2) + \lambda\|\boldsymbol{D\beta}\|^2 \tag{9}$$

Examples of IRLS are qTONE presented in [23] and dTONE method in [24]. These iterative methods use regularization that penalizes small valued predictors producing a more sparse solution compared to OLS and ridge regression. However, similar to lasso method, the ultrasound images produced by qTONE lack uniformity in high speckle regions (see Fig. 3(f)) especially when the imaging grid density is low compared to scatterer density (i.e., dx and dz much larger than the average distance between scatterers in the speckle producing region).

The regularization technique called elastic net [5] takes into account the drawbacks of the lasso method and has shown to outperform the lasso in terms of prediction accuracy for data sets with a large number of predictors. The LARS-EN algorithm described in [5] is used for computing the elastic net regularization paths and has computational complexity similar to a single OLS fit. As such, it significantly outperforms the IRLS methods including qTONE in terms of computational costs and convergence speed (typically by a factor equal to the number of iterations in IRLS). The elastic net optimization problem can be expressed as in (10), where λ is the regularization parameter and $P_\alpha(\boldsymbol{\beta})$ is the penalty function.

$$\begin{aligned}\hat{\boldsymbol{\beta}} &= \underset{\boldsymbol{\beta}}{argmin}(\|\mathbf{y}-\boldsymbol{A\beta}\|^2) + \lambda P_\alpha(\boldsymbol{\beta}),\\ P_\alpha(\boldsymbol{\beta}) &= 0.5(1-\alpha)\|\boldsymbol{\beta}\|^2 + \alpha\|\boldsymbol{\beta}\|_1\end{aligned} \tag{10}$$

The elastic net penalty, $P_\alpha(\boldsymbol{\beta})$, in (10) is a convex combination of lasso and ridge penalty, where $\alpha \in [0, 1)$ represents the weight of lasso (L1-norm) versus ridge regression (L2-norm).

4. Simulation results

To demonstrate the proposed UCI approach for super-resolution imaging, we set up simulations with the help of the open source Field-II toolbox [38,39] in MATLAB environment. A two-dimensional (x-z) grid was setup in a medium with properties similar to homogeneous tissue (c = 1540 m/s and density = 1000 kg/m^3). A 16 element ultrasound probe with a center frequency of 2.5 MHz, pitch of 0.739 mm, height of 0.62 mm and kerf of 0.123 mm was used. Since UCI is based on plane wave excitation, no apodization or dynamic focusing was applied on either transmit or receive. A grid of size $N_x = 21$ and $N_z = 41$ is formed with grid points spaced 0.5 mm in the lateral direction and 0.25 mm in the axial direction corresponding to a 10 mm by 10 mm field of view. We store the impulse response of each of these points on the grid to generate imaging matrix $\boldsymbol{A}$. The phantom used for simulations starts at a depth of 57 mm with a 2 mm radius anechoic cyst centered at 60 mm. The phantom is 6 mm wide and 6 mm deep with the speckle region containing about ten point-scatterers per wavelength squared.

Next, we compare how the estimators described in Section 3 perform in terms of image quality when used to image the anechoic cyst phantom. In conventional DAS method, Contrast Ratio (CR) and Energy Ratio (ER) are typically used to quantify the ultrasound image quality. The CR is defined in (11), where S_{sp} and S_{cyst} are the mean values of the estimated scatterers within the speckle region and the cyst region, respectively. The ER (sometimes called power ratio) is simply defined as the ratio of the energy of the estimated scatterers within the cyst region (E_{cyst}) to that of the surrounding speckle region (E_{sp}), as in (12). The energy measures within the two regions are defined in (13), where N_{cyst} and N_{sp} are the total number of grid points in the cyst and speckle region, respectively. The ER metric proves useful in comparing images in terms of uniformity, where lower ER indicates better uniformity over the region of interest and more clear cyst boundary.

$$CR = \frac{|S_{cyst}-S_{sp}|}{|S_{cyst} + S_{sp}|} \tag{11}$$

$$ER = 20*log_{10}\left(\frac{E_{cyst}}{E_{sp}}\right) \tag{12}$$

$$E_{cyst} = \frac{1}{N_{cyst}}\sum_{\beta_{i,j}\in cyst}\beta_{i,j}^2,\quad E_{sp} = \frac{1}{N_{sp}}\sum_{\beta_{i,j}\in sp}\beta_{i,j}^2 \tag{13}$$

Fig. 3 shows the reconstructed images using OLS, IRLS, ridge regression, lasso and elastic net for $dx = 0.5$ mm and $dz = 0.25$ mm. All estimated images shown are log-compressed to 50 dB scale and interpolated by a factor of 10 for better viewing with the help of cubic interpolation. Also, for each of the estimation methods that permit the use of regularization parameters (e.g., IRLS, lasso, ridge regression, and elastic nets), the parameters are chosen to maximize CR. It is clear that elastic net provides the best estimation of anechoic cyst phantom in terms of CR and ER as compared to other estimation methods (refer to subcaptions in Fig. 3 for each method's CR and ER value). When using lasso, the estimation algorithm tends to cluster the coefficients in certain areas while ridge regression produces result that have values for more less every grid point being estimated. OLS also gives results similar to the ridge method. The IRLS technique implemented here is configured similarly to the qTONE method in [23] and with a proper choice of the regularization parameter σ, provides results close to but not as good as elastic nets. However, the elastic nets method computes at much faster speeds compared to IRLS since the computation time of IRLS depends on the number of iterations required for the results to converge. For example, in MATLAB environment and for the images shown in Fig. 3(g), the elastic nets converges to the solution in 0.3 s while the qTONE method takes about 7 iterations to converge to the solution in 6 s for the same imaging variables.

The effect of the regularization parameter λ and sparsifying parameter α on the image contrast are shown in Figs. 4 and 5 for a grid with $dx = 0.5$ mm and $dz = 0.0625$ mm. Fig. 4 shows how the estimated images vary for a fixed $\lambda = 0.007$ and for $\alpha = 0.1,\ 0.7,\ 0.9$. As α increases, the cyst region clears up and the contrast ratio increases and at the surrounding tissue tends to be more sparse since a higher α means that the L1-norm has more weight during estimation. The ER is the most unfavorable for the first image since there are more estimated scatterers within the cyst region. On the other hand, ER is close to -36 dB for Fig. 4(b) and (c) which indicates a good energy ratio between the two regions in the phantom. Based on ER and CR, the best estimate of the phantom would be Fig. 4(b). Fig. 5 shows the estimated images for a fixed $\alpha = 0.7$ and $\lambda = 0.017,\ 0.007,\ 0.0001$. For lower values of λ as shown in Fig. 5(c), the CR and ER values are lower than desired which makes very low values of λ undesirable. For $\lambda \geqslant 0.01$, the estimated images start getting sparse and do not hold a well defined boundary around the cyst region as shown in Fig. 5(a). A larger phantom with two anechoic cysts and a hyperechoic cyst was imaged using the elastic nets method with $\alpha = 0.4$, $\lambda = 0.005$ and a grid size of $dx = 0.25$ mm, $dz = 0.0625$ mm. The result is shown in Fig. 6.

The point spread function (PSF) for this method is found by moving a point scatterer between two grid points at a depth of 60 mm. The PSF shown in Figs. 7 and 8 is calculated by averaging the results over a few different Φ. Simulations were performed for different grid spacing and it was concluded that grid spacing does not affect the image quality of diffuse targets in terms of CR and ER. However, it affects the resolution as shown by the PSF in Fig. 8. The lateral resolution is limited by the grid spacing (i.e. FWHM = dx) but as the dx becomes smaller, the FWHM does not decrease at the same rate for a given choice of sparsity

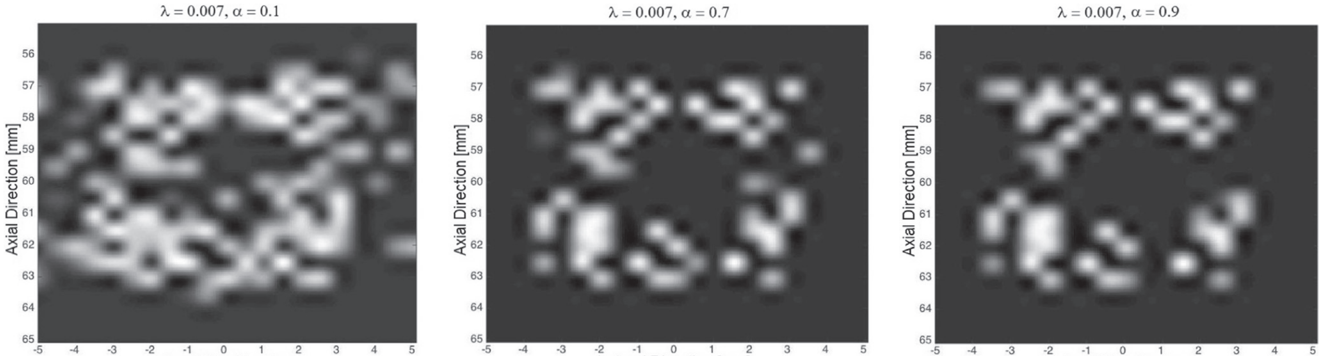

(a) Elastic nets $\lambda = 0.007$,$\alpha = 0.1$: CR = 0.64, ER = -9.82 dB

(b) Elastic nets $\lambda = 0.007$,$\alpha = 0.7$: CR = 0.944, ER = -36.66 dB

(c) Elastic nets $\lambda = 0.007$,$\alpha = 0.9$: CR = 0.941, ER = -36.39 dB

Fig. 4. Images Estimated using α = 0.1, 0.7, 0.9 and λ = 0.007.

parameter α. Since many factors such as λ, α, sampling frequency, and inherent non-linearity of the elastic nets affect the FWHM, finding a closed form expression for a fundamental limit on resolution of the UCI method is a non-trivial task. Therefore, more detailed numerical analysis would be required, which is out of scope of this paper.

5. Experimental results

For further proof of concept, we performed a few experiments using the Verasonics V1 128Tx/64Rx ultrasonic scanner connected to a 96 channel phased array ATL probe, P4-1 with center frequency of 2.5 MHz and a total aperture size of 28 mm. Since the scanner was able to support only 64 channels on receive after single pulse excitation, we used only the first half of the transducer's aperture (48 channels spanning 14.16 mm) to obtain traditional DAS images. For the proposed UCI method, we decided to use the first 16 elements of the probe. This choice is based on a trade-off between the desired high compression ratio and image quality (i.e., choosing larger array would result in lower data rates but degraded image quality due to the compression loss). The probe is placed roughly 9 cm above the target phantom. In order to demonstrate UCI's super-resolution imaging capability, we set the excitation frequency to the lowest frequency 1.875 MHz supported by the P4-1 probe and the scanner that still provides reasonable power. This corresponds to a wavelength of 0.833 mm at a speed of 1540 m/s. This choice of low excitation frequency (and correspondingly large wavelength) allows for a better control over the experimental setup and more manageable phantom construction. It should be noted that even though 1.875 MHz is not typically used in medical ultrasound, it provides proof of concept that readily scales to higher frequencies. It should also be noted that, in this work, super-resolution is defined as the imaging system's ability to resolve spatial features below Abbe's diffraction limit $\lambda/(2NA)$, where *NA* is the system's numerical aperture.

Raw RF data is collected and then passed through a finite impulse response bandpass filter in MATLAB which removes any noise outside the bandwidth of interest. This is followed by the image reconstruction algorithm. Note that we do not apply apodization, focusing and beamforming. The impulse response from different grid points were obtained by moving the transducer probe along the x and z dimensions with the help of a manual xyz positioning stage and the point scatterer used was a single stationary fishing wire in water tank at about 9.1 cm depth. The fishing wire had a diameter of 0.2 mm, which is roughly a quarter of the wavelength or less than $\frac{1}{10}$th the conventional diffraction limit. The grid points were taken 0.4 mm apart in both the axial and lateral direction for the experiments performed.

The first experiment conducted consisted of a target made of two nylon wires of diameter 0.2 mm separated by 0.8 mm laterally and immersed in a water bath. The grid size assumed for this experiment was 3.6 mm by 2.0 mm with each grid point separated by 0.4 mm both axially and laterally, which is about a half of the wavelength. The UCI image is shown in Fig. 9(b). The images estimated by the UCI have four pixels per wavelength squared, but is shown here interpolated to 40 pixels for better viewing. For this purpose we use cubic interpolation since it does not affect the actual data points as shown in Fig. 9(c). Note that all images shown in this section are log-compressed to a 50 dB scale. Some background noise is visible in the images and can be reduced by averaging the reconstructed images. The UCI image is compared to those obtained using conventional DAS method available with the Verasonics ultrasonic scanner. The DAS setup uses synthetic aperture imaging with two apertures with each aperture consisting of 48 elements as well as rectangular apodization and fixed focusing on

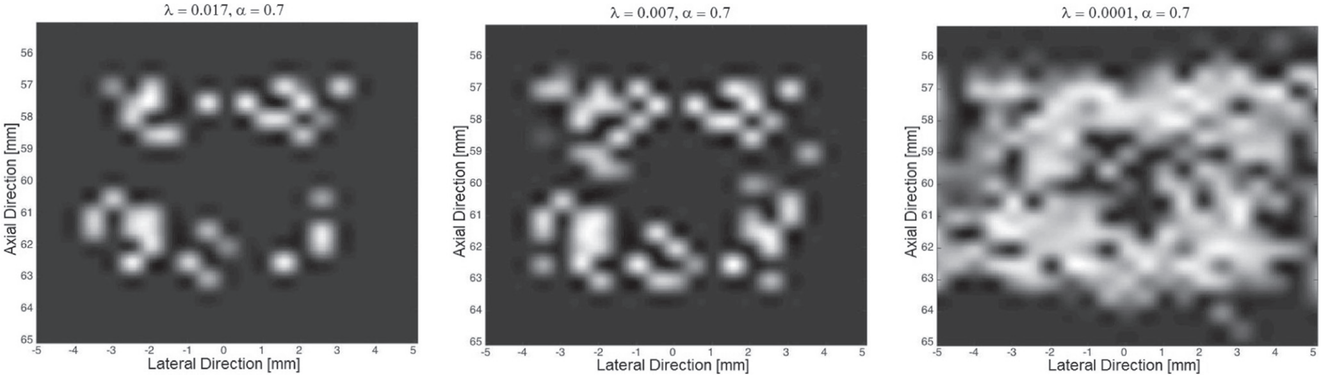

(a) Elastic nets $\lambda = 0.017$,$\alpha = 0.7$: CR = 0.884, ER = -22.05 dB

(b) Elastic nets $\lambda = 0.007$,$\alpha = 0.7$: CR = 0.944, ER = -36.66 dB

(c) Elastic nets $\lambda = 0.0001$,$\alpha = 0.7$: CR = 0.771, ER = -13.95 dB

Fig. 5. Images Estimated using α = 0.7 and λ = 0.017, 0.007, 0.0001.

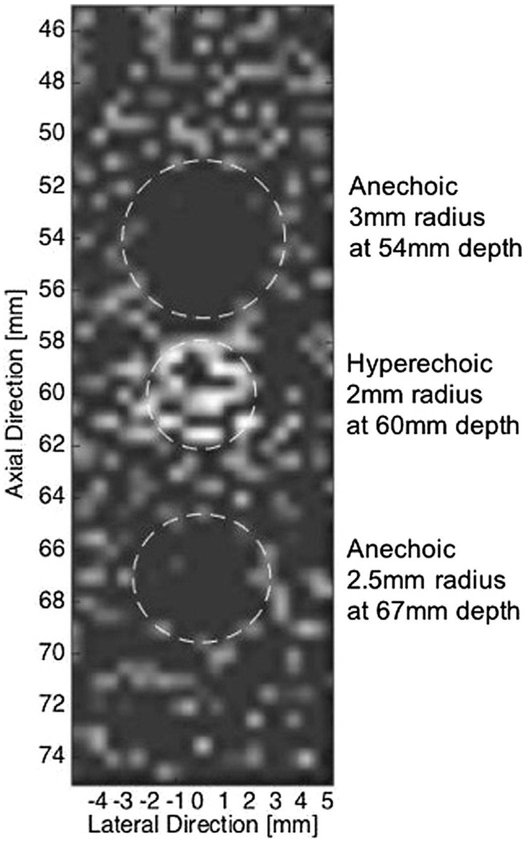

Fig. 6. Estimated image of a cyst phantom with hyperechoic and anechoic cysts.

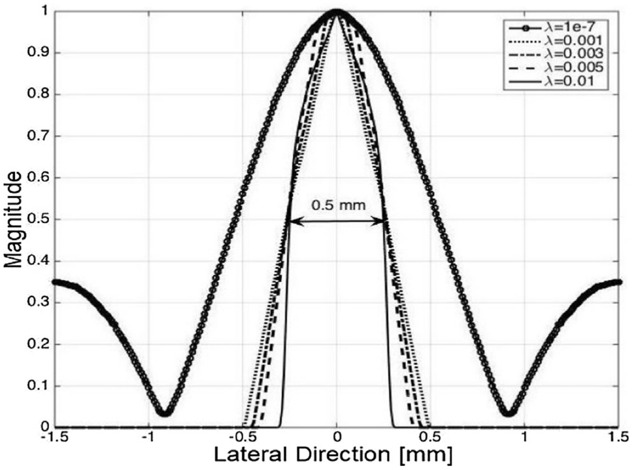

Fig. 7. Point Spread Function for various λ.

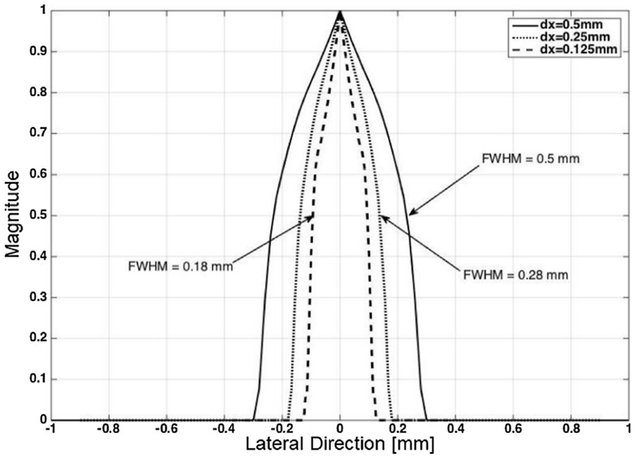

Fig. 8. Point Spread Function for various grid spacing dx. $\lambda = 0.01$ and $\alpha = 0.8$.

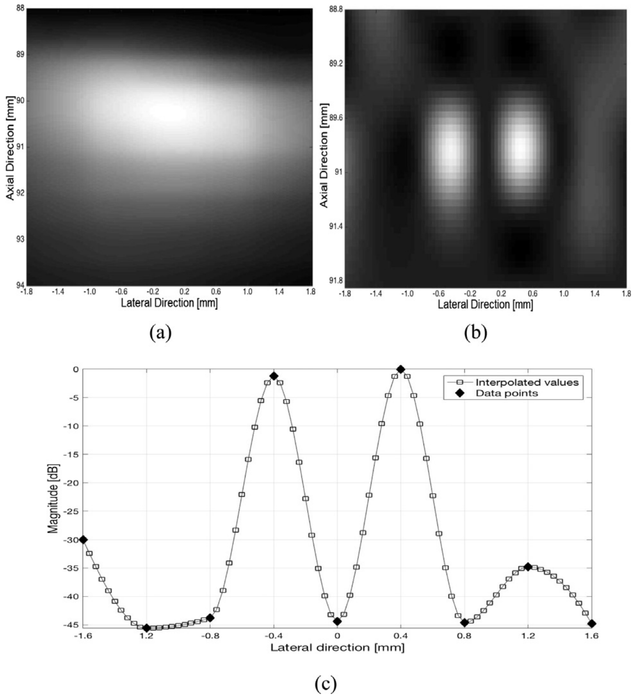

(a)

(b)

(c)

Fig. 9. Experimental results from imaging two wires separated by 0.8 mm laterally. (a) Shows the zoomed in and interpolated DAS image, (b) is the estimated image using UCI, (c) is the lateral magnitude profile of the UCI image at 90 mm depth.

transmit. The scanning method employed is virtual apex imaging with 6 sectors spanning an angle of 45°. It also applies dynamic-focus beamforming on receive. Time gain compensation is applied for both DAS and UCI during receive. Fig. 9(a) shows a DAS image of the same two-wire imaging target interpolated (cubic interpolation) to 40 pixels per wavelength squared. Note that at this frequency (1.875 MHz), the diffraction limit is calculated to be 2.7 mm for the full aperture (28 mm). Clearly, the two wires cannot be distinguished in the DAS image, while the UCI image shows clear distinction despite using only half the aperture (corresponding to a diffraction limit of 5.4 mm). Fig. 9(c) shows a lateral brightness profile at the depth of 90 mm from Fig. 9(b) illustrating both data points obtained by the UCI method and interpolated points. It should be noted that the data point centered in between the two wires has a brightness level that is about 45 dB below the data point corresponding to the wire location demonstrating the method's ability to resolve the two point targets. Another key feature of our method is the absence of side lobes due to its non-focusing nature, which helps to improve the resolution.

For a more realistic imaging scenario, an experiment was performed to see the resolution capability of the UCI technique behind a living tissue. This was performed using a piece of steak of 1 cm thickness. Beef has an acoustic impedance of 1.68×10^5 g/cm^2 sec and a density of 1.08 g/cm^3. As can be seen in Fig. 10(a), the signal is attenuated due to the tissue layer above the wires while the resolution is clearly maintained. In another set of experiments, a set of 3 fishing wires is imaged as shown in Fig. 10(b). The wires were spanned at random locations within the field of view, not necessarily corresponding to the grid locations. As it can be seen from Fig. 10(b), the received echo from the

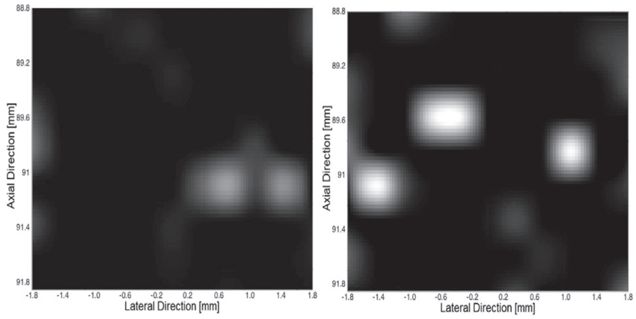

(a) 2-wire phantom behind a tissue (b) 3-wire phantom

Fig. 10. UCI experimental results. (a) Shows an image of two wires separated by 0.8 mm behind a 1 cm thick beefsteak placed at 3 cm depth, (b) shows a UCI image of three parallel wires.

middle wire is confined to the nearest neighboring grid points indicating a PSF that is as narrow as the distance between the two grid points $dx = 0.4$ mm.

Next, an anechoic cyst phantom was made in a gel substance with properties similar to tissue. The gel was created using 2% copper sulphate, 2% cornstarch, 2% agar, 20% gelatin and 74% water by mass. Cornstarch was added to mimic scatterers in living tissue. The cyst was roughly 2.2 mm in diameter. For visualization and phantom quality assessment purposes, we first imaged the cyst phantom with Verasonic's DAS method at 7.5 MHz by using an ATL L12-5 linear array. The cyst was centered at a depth of roughly 17 mm and the resulting image is shown in Fig. 11(a). Then, we imaged the same phantom with DAS at 1.875 MHz with the same setup used for imaging the wire phantom. The cyst was centered much deeper at roughly 9.1 cm and the resulting image is shown in Fig. 11(b).

To evaluate imaging performance of the UCI method, a grid of size of 5.2 mm × 5.2 mm was generated with a grid spacing of 0.4 mm in both lateral and axial directions. The cyst in Fig. 12(b) estimated using elastic nets showed a CR of 0.96 and ER of -38 dB. On the other hand, the DAS anechoic cyst produces an ER of -15 dB and CR of 0.62 which is validated by the reduced ability to distinguish the cyst region from its surrounding speckle region as shown in Fig. 12(a).

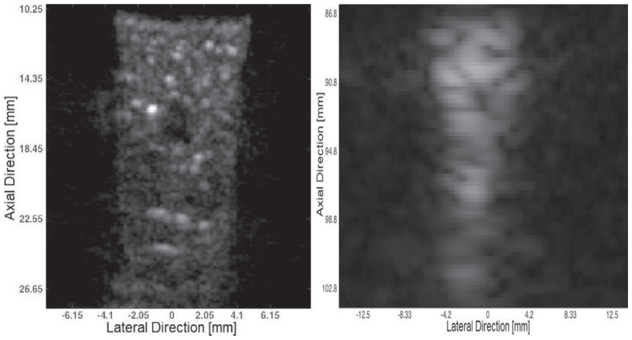

(a) f_c = 7.5 MHz (b) f_c = 1.875 MHz

Fig. 11. Experimental results from imaging an anechoic cyst phantom in DAS method. (a) shows image of the cyst phantom centered at 17 mm with 7.5 MHz excitation frequency, (b) shows the cyst placed deeper at 91 mm with 1.875 MHz.

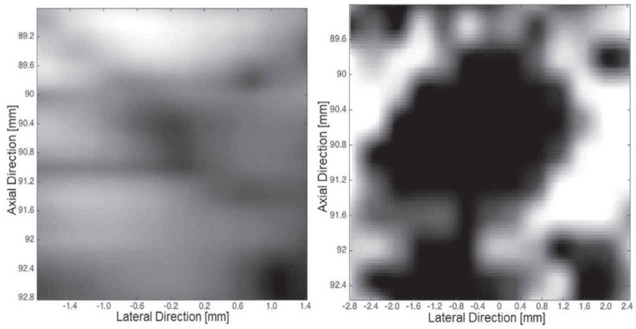

(a) DAS method (b) UCI method

Fig. 12. Experimental results from imaging an anechoic cyst phantom @ 1.875 MHz. (a) DAS method with CR = 0.62, ER = -15 dB, (b) UCI method with CR = 0.96, ER = -38 dB.

Table 1
Comparison of resolution gain for different methods.

Super-resolution Method	Resolution Gain
PC-MUSIC [15]	3
Semi-blind deconvolution [40]	2.78
2-D blind homomorphic deconvolution [17]	2–4
Spatially-variant deconvolution [41]	5.1
Minimum variance beamforming [8]	4
UCI	13

6. Discussion

To get a better insight into the performance of the UCI, Table 1 provides the resolution gain comparison between different super-resolution techniques. The resolution gain here is defined with respect to conventional B-mode method with DAS. As it can be seen, the UCI method presents a resolution improvement by at least a factor of 2.5 in comparison to other super-resolution methods discussed in here. The UCI method achieves similar resolution gain to other model based imaging methods such as qTONE in [23] and dTONE in [24]. However, unlike qTONE and dTONE, the UCI method requires much reduced memory storage and computational power thanks to its compressive nature and the use of elastic nets. For example, in MATLAB environment and for the images shown in Fig. 3, the elastic nets converges to the solution in 0.3 s while the qTONE method takes about 6 s for the same imaging variables. Another important benefit of the UCI should be noted here. Since the UCI creates an entire image after a single plane wave excitation, it has a potential to be much faster than traditional DAS and, therefore, less affected by motion artifacts. With the help of a smaller grid spacing and higher frequencies, higher resolution images than those demonstrated, can be obtained. One possible issue is the need for a larger memory to store the pseudo-random modulation matrix ϕ. Once the grid size grows, the regularized estimation problem could slow down but techniques such as singular value decomposition of the **A** matrix defined in (6) can speed up the process. Computational power available in present portable and mobile platforms may not be sufficient for performing regularized estimation and reconstruction of large grid size images with reasonable speed rendering UCI's portable implementations with local computing impossible. However, a genuinely portable solution can be achieved by communicating compressed RF data to servers and utilizing cloud computing resources for computationally intensive estimation of a large matrix in a smaller time frame. For example, if we assume an imaging depth of 10 cm with excitation frequency of 2.5 MHz with the sampling rate of 8 samples per wavelength, the UCI would produce about 1300 12-bit samples per channel or a total of 30 Kb per exposure. If we also assume a video rate of 30 frames per second, the resulting data rate is 900 Kb/sec, which can be readily transferred over a Wi-Fi or LTE to cloud servers for image estimation. Estimated images would then be streamed back to the portable unit for display, which is also readily achievable with present video streaming technology. Nevertheless, future work needs to be carried out in order to characterize our method for larger grid sizes in terms of decoding time and memory requirements.

Research is also needed to pre-calculate the imaging matrix '**A**' rather than experimentally determining the compressed RF data entries while analyzing the effect of image artifacts at the same time. Future work will also be directed at evaluating the performance of the UCI method for living tissue and the presence of multi-path and off axis signals. The availability of a portable and inexpensive ultrasound system capable of providing high-resolution images will help with easy diagnosis in case of field emergency and trauma.

7. Conclusion

We present a coherent ultrasound imaging technique which takes into account the phase of the received RF signal on top of the amplitude. The method not only provides super-resolution but also incorporates compression, thereby reducing the analog and digital data footprint making it attractive for portable ultrasound systems. We provide simulation and experimental results validating the image reconstruction technique.

Our coherent imaging technique was able to distinguish two wire scatterers placed one wavelength apart at a depth of 9.1 cm at a frequency of 1.875 MHz. This corresponds to a spatial resolution that is about 13 times higher than the spatial resolution of conventional B-mode with delay and sum. We were also able to image an anechoic cyst phantom of 2.2 mm with a contrast ratio of 0.96 and energy ratio of −38 dB at the same depth and center frequency.

References

[1] E.J. Candes, T. Tao, Decoding by linear programming, IEEE Trans. Informat. Theory 51 (12) (2005) 4203–4215.

[2] S. George, R. Cheng, Z. Ignjatovic, A novel ultrasound imaging technique for portable and high speed imaging, New Circuits and Systems Conference (NEWCAS), 2015 IEEE 13th International, IEEE, 2015, pp. 1–4.

[3] Z. Ignjatovic, M. Huang, S. George, Ultrasound system for high-speed and high resolution imaging applications, Jun. 23 2016, wO Patent App. PCT/US2015/065, 722. [Online]. Available: < http://google.com/patents/WO2016100284A1?cl=en > .

[4] S. George, A. Anand, J. Mitrovic, Z. Ignjatovic, Low-complexity compressive beamforming for portable ultrasound imaging, in: 2017 IEEE International Ultrasonics Symposium (IUS), Sept 2017.

[5] H. Zou, T. Hastie, Regularization and variable selection via the elastic net, J. Roy. Stat. Soc.: Ser. B (Stat. Methodol.) 67 (2) (2005) 301–320.

[6] O. Michailovich, D. Adam, Phase unwrapping for 2-d blind deconvolution of ultrasound images, IEEE Trans. Med. Imag. 23 (1) (2004) 7–25.

[7] T. Taxt, G.V. Frolova, Noise robust one-dimensional blind deconvolution of medical ultrasound images, IEEE Trans. Ultrason. Ferroelectr. Freq. Control 46 (2) (1999) 291–299.

[8] J.-F. Synnevåg, A. Austeng, S. Holm, Benefits of minimum-variance beamforming in medical ultrasound imaging, IEEE Trans. Ultrason. Ferroelectr. Freq. Control 56 (9) (2009) 1868–1879.

[9] S. Holm, J. Synnevag, A. Austeng, Capon beamforming for active ultrasound imaging systems, in: Proc. IEEE, 13th DSP Workshop, 2009.

[10] J.A. Mann, W. Walker, A constrained adaptive beamformer for medical ultrasound: initial results, Ultrasonics Symposium, 2002. Proceedings. 2002 IEEE, vol. 2, IEEE, 2002, pp. 1807–1810.

[11] I.K. Holfort, F. Gran, J.A. Jensen, P2b-12 minimum variance beamforming for high frame-rate ultrasound imaging, Ultrasonics Symposium, 2007. IEEE, IEEE, 2007, pp. 1541–1544.

[12] B.M. Asl, A. Mahloojifar, Eigenspace-based minimum variance beamforming applied to medical ultrasound imaging, IEEE Trans. Ultrason. Ferroelectr. Freq. Control 57 (11) (2010) 2381–2390.

[13] P. Blomgren, G. Papanicolaou, H. Zhao, Super-resolution in time-reversal acoustics, J. Acoust. Soc. Am. 111 (1) (2002) 230–248.

[14] A.J. Devaney, Super-resolution processing of multi-static data using time reversal and music, 2000. [Online]. Available: < https://www.ece.neu.edu/fac-ece/devaney/preprints/paper02n_00.pdf > .

[15] Y. Labyed, L. Huang, Super-resolution ultrasound imaging using a phase-coherent music method with compensation for the phase response of transducer elements, IEEE Trans. Ultrason. Ferroelectr. Freq. Control 60 (6) (2013) 1048–1060.

[16] T. Dertinger, R. Colyer, R. Vogel, J. Enderlein, S. Weiss, Achieving increased resolution and more pixels with superresolution optical fluctuation imaging (SOFI), Opt. Express 18 (18) (2010) 18875–18885.

[17] T. Taxt, R. Jiřík, Superresolution of ultrasound images using the first and second harmonic signal, IEEE Trans. Ultrason. Ferroelectr. Freq. Control 51 (2) (2004) 163–175.

[18] D. Kouame, M. Ploquin, Super-resolution in medical imaging: an illustrative approach through ultrasound, Biomedical Imaging: From Nano to Macro, 2009. ISBI'09. IEEE International Symposium on, IEEE, 2009, pp. 249–252.

[19] Y. Yankelevsky, Z. Friedman, A. Feuer, Component based modeling of ultrasound signals, CoRR, 2016. Available from: < 1603.00273 > .

[20] N. Wagner, Y.C. Eldar, A. Feuer, G. Danin, Z. Friedman, Xampling in ultrasound imaging, in: SPIE Medical Imaging. International Society for Optics and Photonics, 2011, pp. 796818–796818.

[21] M. Vetterli, P. Marziliano, T. Blu, Sampling signals with finite rate of innovation, IEEE Trans. Signal Process. 50 (6) (2002) 1417–1428.

[22] B. Byram, K. Dei, J. Tierney, D. Dumont, A model and regularization scheme for ultrasonic beamforming clutter reduction, IEEE Trans. Ultrason. Ferroelectr. Freq. Control 62 (11) (2015) 1913–1927.

[23] M.A. Ellis, W.F. Walker, Super-resolution image reconstruction with reduced computational complexity, 2009 IEEE International Ultrasonics Symposium, IEEE, 2009, pp. 2351–2354.

[24] M.A. Ellis, F. Viola, W.F. Walker, Super-resolution image reconstruction using diffuse source models, Ultrasound Med. Biol. 36 (6) (2010) 967–977.

[25] R. Lavarello, F. Kamalabadi, W.D. O'Brien, A regularized inverse approach to ultrasonic pulse-echo imaging, IEEE Trans. Med. Imag. 25 (6) (2006) 712–722.

[26] T. Szasz, A. Basarab, M.-F. Vaida, D. Kouamé, Elastic-net based beamforming in medical ultrasound imaging, Biomedical Imaging (ISBI), 2016 IEEE 13th International Symposium on, IEEE, 2016, pp. 477–480.

[27] G. Clement, J. Huttunen, K. Hynynen, Superresolution ultrasound imaging using back-projected reconstruction, J. Acoust. Soc. Am. 118 (6) (2005) 3953–3960.

[28] K.K. Sharma, Optics: Principles and Applications, Academic Press, 2006.

[29] B.R. Hunt, Super-resolution of imagery: understanding the basis for recovery of spatial frequencies beyond the diffraction limit, Information, Decision and Control, 1999. IDC 99. Proceedings, IEEE, 1999, pp. 243–248.

[30] E.J. Candès and C. Fernandez-Granda, Towards a mathematical theory of super-resolution, CoRR, 2012. Available from: < 1203.5871 > .

[31] M. Schiffner, T. Jansen, G. Schmitz, Compressed sensing for fast image acquisition in pulse-echo ultrasound, Biomed. Eng./Biomedizinische Technik 57 (SI-1 Track-B) (2012) 192–195.

[32] F. Lingvall, A method of improving overall resolution in ultrasonic array imaging using spatio-temporal deconvolution, Ultrasonics 42 (1) (2004) 961–968.

[33] A. Hoerl, R. Kennard, Ridge regression, in: Encyclopedia of Statistical Sciences, vol. 8, 1988.

[34] T. Szasz, A. Basarab, D. Kouamé, Beamforming through regularized inverse problems in ultrasound medical imaging, IEEE Trans. Ultrason. Ferroelectr. Freq. Control 63 (12) (2016) 2031–2044.

[35] R. Tibshirani, Regression shrinkage and selection via the lasso, J. Roy. Stat. Soc. Ser. B (Methodol.) (1996) 267–288.

[36] L.L. Scharf, Statistical Signal Processing, Addison-Wesley, Reading, MA, 1991.

[37] P.J. Green, Iteratively reweighted least squares for maximum likelihood estimation, and some robust and resistant alternatives, J. Roy. Stat. Soc. Ser. B (Methodol.) (1984) 149–192.

[38] J.A. Jensen, Field: a program for simulating ultrasound systems, in: 10th NordicBaltic Conference On Biomedical Imaging 4 1. Citeseer, 1996, pp. 351–353.

[39] J.A. Jensen, N.B. Svendsen, Calculation of pressure fields from arbitrarily shaped, apodized, and excited ultrasound transducers, IEEE Trans. Ultrason. Ferroelectr. Freq. Control 39 (2) (1992) 262–267.

[40] R. Morin, S. Bidon, A. Basarab, D. Kouame, Semi-blind deconvolution for resolution enhancement in ultrasound imaging, 2013 IEEE International Conference on Image Processing, IEEE, 2013, pp. 1413–1417.

[41] J.A. Jensen, Real time deconvolution of in-vivo ultrasound images, 2013 IEEE International Ultrasonics Symposium (IUS), IEEE, 2013, pp. 29–32.

Swetha S. George received the bachelors degree in electronics and telecom engineering from Mahatma Gandhi University, Kerala, India, in 2010, and the M.S. degree in electrical and telecom engineering from Drexel University, PA, USA. She is currently pursuing the Ph.D. degree in electrical and computer engineering at the University of Rochester, NY, USA, where she is also a Research Assistant under Dr. Z. Ignjatovic. Her research interests include image sensors, analog design, digital image processing.

Michael C. Huang (M'02) received the BS degree in computer science and engineering from Tsinghua University, Beijing, China, in 1994, and the MS and PhD degrees in computer science from University of Illinois, Urbana-Champaign, in 1999 and 2002, respectively. From 1994 to 1997, he was a lead architect in building a 32-processor hierarchical shared-memory multiprocessor research prototype. He joined the faculty of the Electrical and Computer Engineering Department, University of Rochester, in 2002. In 2010, he was on sabbatical at IBM T.J. Watson Research Center working on Future Power Processor Concept Development. His research interests include various aspects of high-performance computing.

Zeljko Ignjatovic (M'01) received the B.S. degree in electrical engineering from the University of Novi Sad, Serbia, in 1999, and the M.S. and Ph.D. degrees in electrical engineering from the University of Rochester, NY, USA, in 2001 and 2004, respectively. He is currently an Associate Professor of Electrical and Computer Engineering with the University of Rochester. His areas of interest include analog circuit design and development of analog-to-digital converters, image sensor architectures, radar and ultrasound imaging techniques, and related signal processing methods.